https://doi.org/10.5194/egusphere-2026-5957
Preprint. Discussion started: 3 November 2026
© Author(s) 2026. CC BY 4.0 License.

Evaluation of the new near-infrared (1625 nm) aerosol optical depth product from the upgraded Multifilter Rotating Shadowband Radiometers (MFRSRs)

Evgueni Kassianov[1], Connor J. Flynn[2], Erol L. Cromwell[1], Gabe L. Gibler[1], John A. Augustine[3], Joseph J. Michalsky[3], Gary Hodges[3,4], Benjamin R. Sheffer[3,4], Hagen Telg[3,4], Lihong Ma[5], James C. Barnard[6], John E. Shilling[1], Damao Zhang[1], Jennifer M. Comstock[1]

[1] Pacific Northwest National Laboratory, Richland, Washington, USA
[2] School of Meteorology, University of Oklahoma, Norman, Oklahoma, USA
[3] NOAA Global Monitoring Laboratory, Boulder, Colorado, USA
[4] Cooperative Institute for Research in Environmental Sciences, University of Colorado, Boulder, Colorado, USA
[5] Brookhaven National Laboratory, Upton, New York, USA
[6] Department of Physics, University of Nevada, Reno, Nevada, USA

Correspondence to: Evgueni Kassianov (Evgueni.Kassianov@pnnl.gov)

Abstract. This study evaluates a new near-infrared (1625 nm) aerosol optical depth (AOD) product generated from data provided by upgraded Multifilter Rotating Shadowband Radiometers (MFRSRs). The generation of the new AOD product involves spectral integration of solar transmittance, line-by-line gas absorption spectra, and instrumental filter response function. The evaluation of the new AOD utilizes datasets from four fixed Atmospheric Radiation Measurement (ARM) sites: Southern Great Plains (SGP C1, SGP E13), North Slope of Alaska (NSA C1), and Eastern North Atlantic (ENA C1). Additionally, datasets collected during seven ARM field campaigns are incorporated: (1) Bankhead National Forest (BNF M1), (2) Cloud And Precipitation Experiment at Kennaook (CAPE-k), (3) Coast-Urban-Rural Atmospheric Gradient Experiment (CoURAGE), (4) Eastern Pacific Cloud Aerosol Precipitation Experiment (EPCAPE), (5) Surface Atmosphere Integrated Field Laboratory (SAIL), (6) Tracking Aerosol Convection Interactions Experiment (TRACER), and (7) Oliktok Point (OLI). Datasets from National Oceanic and Atmospheric Administration (NOAA) Surface Radiation Budget (SURFRAD) Table Mountain Test Facility are also utilized. Using coincident 1640 nm AODs measured by collocated AERONET (Aerosol Robotic Network) Cimel sun photometers as a reference, we assess the 1625 nm MFRSR AODs across diverse environments with moderate-to-high cloud cover. Despite frequent cloud presence, the 1625 nm MFRSR AOD correlates strongly with the AERONET data, clustering tightly along the 1:1 line across nearly all deployments. The corresponding linear regressions yield slopes close to unity, root-mean-square errors (RMSEs) mostly below 0.013, and absolute biases within 0.01. Furthermore, we demonstrate that excellent agreement between the MFRSR and AERONET AOD values can be achieved under near-ideal operational conditions characterized by a high clear-sky frequency, rigorous instrument calibration, and meticulous maintenance: under these optimal conditions an ideal linear regression slope of 1.00 and an exceptionally low RMSE of 0.004 are obtained.

https://doi.org/10.5194/egusphere-2026-5957
Preprint. Discussion started: 3 November 2026
© Author(s) 2026. CC BY 4.0 License.

1 Introduction

Over the past several decades, extensive research has evaluated the impacts of natural and anthropogenic aerosols on Earth's radiation budget (e.g., Bellouin et al., 2020; Kalisoras et al., 2024), cloud dynamics (e.g., Gryspeerdt et al., 2016; Riipinen et al., 2026), precipitation (e.g., Risser et al., 2024; Alterskjær et al., 2026), and public health (e.g., Davidson et al., 2005; Damiati et al., 2025). This body of work frequently focuses on two objectives: characterizing aerosol particle size distributions using remote sensing and *in situ* measurements (e.g., Jaegle et al., 2010; Kassianov et al., 2012; Li and Ginoux, 2025; Gilardoni et al., 2026) and quantifying the relative contributions of fine aerosols (FA, radius <1 μm) and coarse aerosols (CA, radius >1 μm) to aerosol–radiation–cloud interactions (e.g., Dusek et al., 2006; Yin et al., 2024; Liu et al., 2025). For instance, Liu et al. (2025) demonstrated that FA and CA (specifically sea spray) exert opposite effects on cloud liquid water path adjustments via precipitation–evaporation competition. Therefore, long-term observational frameworks are essential to systematically quantify FA and CA contributions across diverse environmental regimes.

These quantifications commonly rely on multi-wavelength aerosol optical depth (AOD) retrievals from ground-based networks (e.g., Holben et al, 1998; Nakajima et al., 2020), airborne platforms (e.g., Shinozuka et al., 2011, Wang et al., 2024), and satellite remote sensing (e.g., Sawyer et al., 2025; Levy et al., 2026). Because FA and CA drive the spectral dependence of AOD, a steep spectral gradient characterized by a rapid decrease in AOD with increasing wavelength indicates FA dominance. Conversely, a weak spectral dependence signifies CA dominance, typically associated with desert dust, sea salt, or volcanic ash. AOD measurements at near-infrared (NIR) wavelengths (e.g., 1600-1650 nm) exhibit significantly higher sensitivity to CA than at shorter visible wavelengths (e.g., Laszlo and Liu, 2022), providing a distinct spectral signature for CA identification. Furthermore, ground-based measurements of downwelling and upwelling solar radiation within the NIR spectrum offer unique spectral constraints to classify surface types and derive high-resolution spectral surface albedo (e.g., McFarlane et al., 2011), which can be used to quantify cloud properties from ground-based solar radiation measurements (e.g., Chiu et al., 2006; LeBlanc et al., 2015; Riihimaki et al., 2021).

Several ground-based instruments measure spectral solar irradiance and its diffuse and direct components (e.g., Michalsky et al., 2010; Michalsky and Kiedron, 2022; Balmes et al., 2024; Kassianov et al., 2024; García et al., 2026). The diffuse component represents downwelling solar radiation scattered to the surface from all directions, while the direct-beam component represents solar radiation coming directly from the solar disk. Direct-beam atmospheric transmittance is used to derive AOD at wavelengths where trace gas absorption is small relative to total aerosol extinction (e.g., Michalsky et al., 2010; Balmes et al., 2024; Kassianov et al., 2024). Well-known examples of such instruments for spectral solar irradiance measurements include Multifilter Rotating Shadowband Radiometers (MFRSRs) deployed by the US Department of Energy's Atmospheric Radiation Measurement (ARM) user facility (e.g., Miller et al., 2016; Sisterson et al., 2016; Verlinde et al., 2016;

https://doi.org/10.5194/egusphere-2026-5957
Preprint. Discussion started: 3 November 2026
© Author(s) 2026. CC BY 4.0 License.

Wood et al., 2015) and the National Oceanic and Atmospheric Administration's Surface Radiation Budget network (SURFRAD; e.g., Augustine et al., 2000, 2005).

For nearly three decades, these MFRSRs have recorded total, diffuse, and direct solar irradiance at six filtered wavelengths (415, 500, 615, 673, 870, and 940 nm) and one unfiltered. Standard processing yields AOD at five of these nominal filter wavelengths (excluding 940 nm due to strong water vapor absorption) with a low estimated uncertainty of approximately 0.01 to 0.02. ARM and NOAA upgraded these instruments to incorporate a new NIR channel centred at 1625 nm wavelength. The updated NOAA configuration implemented between 2013-2016 at SURFRAD sites replaced the 614 nm channel with a new NIR channel centred at 1625 nm. The updated ARM configuration, designated as the seven-channel MFRSR (7-ch MFRSR), beginning in 2021 replaced the unfiltered channel yielding total, diffuse, and direct irradiance at seven discrete wavelengths (415, 500, 615, 673, 870, 940, and 1625 nm), extending the derived AOD product to six nominal wavelengths (415, 500, 615, 673, 870, and 1625 nm).

This study presents a new AOD product generated for the 1625 nm narrow-band channel (channel 7) of the upgraded MFRSRs. The underlying methodology builds on the established frameworks (e.g., Ortiz de Galisteo et al., 2009; Korkin et al., 2025). For example, Ortiz de Galisteo et al. (2009) calculated filter-dependent corrections for ultraviolet ozone absorption (340 or 380 nm) for Cimel sun photometers. Here, the calculation of filter-dependent corrections is extended to the NIR spectral region (1625 nm) to account for gas absorption by carbon dioxide, methane, and water vapor. Similar to the established frameworks (e.g., Ortiz de Galisteo et al., 2009; Korkin et al., 2025), the NIR corrections for the 1625 nm MFRSR channel are determined by spectrally integrating the solar transmittance, line-by-line gas absorption spectra, and the instrumental filter response function. This study also compares the 1625 nm MFRSR AOD against collocated AOD measured at 1640 nm by Aerosol Robotic Network (AERONET; Holben et al., 1998) Cimel sun photometers deployed at ARM fixed sites, recent field campaigns, and NOAA Table Mountain Test Facility. The remainder of this paper is structured as follows: Sect. 2 outlines the ground-based measurements across fixed and mobile ARM sites, and NOAA Table Mountain Test Facility; Sect. 3 describes the AOD calibrations and gas corrections, focusing on the MFRSR processing pipeline; Sect. 4 discusses the evaluation of the 1625 nm MFRSR AOD; and Sect. 5 summarizes our primary conclusions.

2 Sites and campaigns

Evaluating a new aerosol product requires accounting for diverse observational conditions across varying aerosol types and cloudiness, while ensuring the availability of high-quality reference data from collocated, independent, and coincident instruments (e.g., Karanikolas et al., 2024). This study satisfies both criteria by utilizing data from four fixed ARM sites, seven ARM Mobile Facility (AMF) campaigns, and NOAA Table Mountain Test Facility conducted across environmentally critical regions. Comprehensive descriptions of these sites, campaigns, and their instrumentation are available via the ARM (e.g., Miller et al., 2016; Sisterson et al., 2016; Verlinde et al., 2016; Wood et al., 2015) and NOAA (e.g., Augustine et al., 2000,

https://doi.org/10.5194/egusphere-2026-5957
Preprint. Discussion started: 3 November 2026
© Author(s) 2026. CC BY 4.0 License.

2005) repositories. This section highlights these locations (Fig. 1) with a specific focus on the datasets used for evaluation: spectrally resolved AODs provided by collocated and coincident MFRSRs and Cimel sun photometers (Table 1).

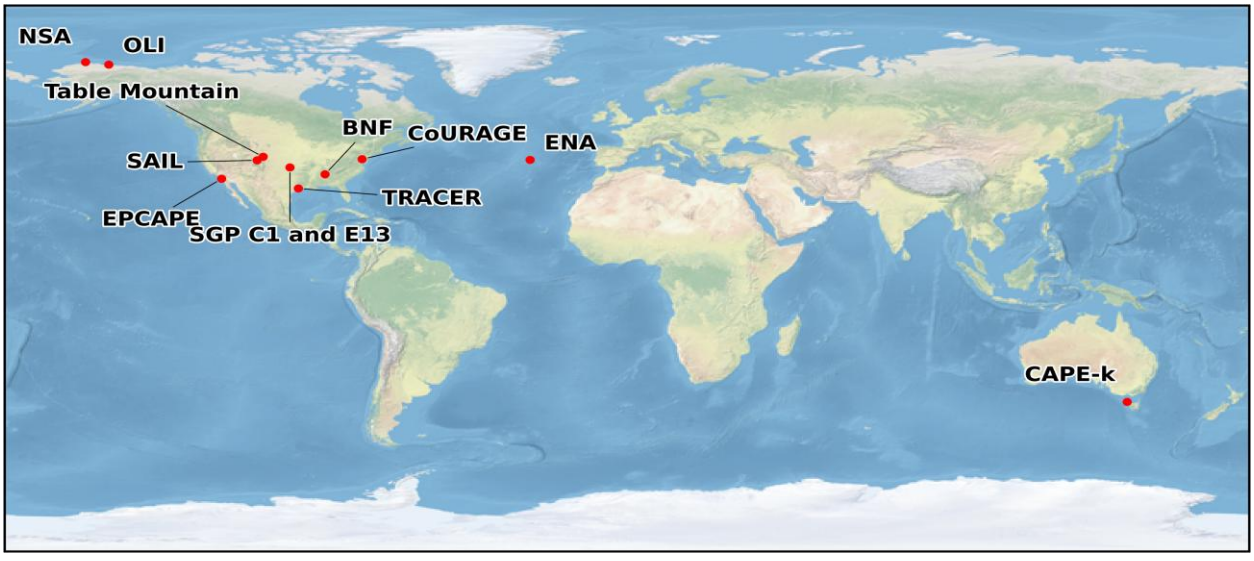


Figure 1. Map of ARM and NOAA deployments (Sects. 2.1 and 2.2) with collocated MFRSR and Cimel sun photometer measurements (Table 1).

2.1 ARM fixed research sites

The fixed ARM sites provide continuous, multi-year measurements of clouds, aerosols, and radiative fluxes across vastly different environmental regimes.

- **Southern Great Plains (SGP):** Located in north-central Oklahoma (USA), this observatory focuses on land–atmosphere interactions, leveraging its wide range of surface and atmospheric conditions. This study utilizes AODs measured by two collocated MFRSRs deployed at the SGP C1 and SGP E13 sites, which are separated by approximately 15 m. The MFRSR data used in this study were collected from 10 May 2021 to 31 July 2026 at SGP C1 site and from 1 January 2021 to 31 July 2026 at SGP E13 site. The collocated comparison data were from AERONET site "ARM_ SGP" (Table 1).
- **North Slope of Alaska (NSA):** Located at Utqiaġvik (formerly Barrow), Alaska (USA), near the Arctic Ocean coast, this observatory focuses on high-latitude cloud, ice, and radiative processes to evaluate the impacts of Arctic warming and sea-ice loss. This study utilizes AODs measured at the central facility (C1). The MFRSR data used in this study were collected from 30 September 2021 to 31 July 2026. The collocated comparison data were from AERONET site "Barrow" (Table 1).
- **Eastern North Atlantic (ENA):** Located on Graciosa Island in the Azores (Portugal), this observatory focuses on marine stratocumulus clouds and aerosol–cloud–precipitation interactions in remote marine environment. This study utilizes AODs measured at the central facility (C1). The MFRSR data used in this study were collected from 15 April

https://doi.org/10.5194/egusphere-2026-5957
Preprint. Discussion started: 3 November 2026
© Author(s) 2026. CC BY 4.0 License.

2021 to 31 July 2026 at C1 site. The collocated comparison data were from AERONET site "ARM_Graciosa" (Table 1).

Table 1. Collocated and concurrent MFRSR and Cimel sun photometer data products by measurement site and period. The data availability section outlines the MFRSR and CSPHOT datastreams and AERONET AODs.

MFRSR site	Duration	MFRSR datastream	CSPHOT datastream	AERONET AOD v3
ARM SGP C1	2021-05-10 to 2026-07-31	sgpmfrsr7nchaod1michC1	sgpcsphotaodfiltqav3C1.a1 sgpcsphotaodfiltv3C1.a1	ARM_SGP lv2 ARM_SGP lv1.5
ARM SGP E13	2021-01-12 to 2026-07-31	sgpmfrsr7nchaod1mich E13	sgpcsphotaodfiltqav3C1.a1 sgpcsphotaodfiltv3C1.a1	ARM SGP lv2 ARM SGP lv1.5
ARM NSA C1	2021-09-30 to 2026-07-31	nsamfrsr7nchaod1mich C1	nsacsphotaodfiltqav3C1.a1 nsacsphotaodfiltv3C1.a1	Barrow lv2 Barrow lv1.5
ARM OLI M1	2021-04-03 to 2021-06-14	olimfrsr7nchaod1mich M1	olicsphotaodfiltqav3M1.a1	ARM_Oliktok_AK lv2
ARM ENA C1	2021-04-15 to 2026-07-31	enamfrsr7nchaod1mich C1	enacsphotaodfiltqav3C1.a1 enacsphotaodfiltv3C1.a1	ARM_Graciosa lv2 ARM_Graciosa lv1.5
ARM BNF M1	2024-09-07 to 2026-07-31	bnfmfrsr7nchaod1mich M1	bnfcsphotaodfiltqav3M1.a1 bnfcsphotaodfiltv3M1.a1	ARM_BNF lv2 ARM_BNF lv1.5
ARM KCG M1	2024-03-15 to 2025-10-13	kcgmfrsr7nchaod1mich M1	kcgcsphotaodfiltqav3M1.a1	ARM_KCG lv2
ARM CRG M1	2024-12-12 to 2025-11-29	crgmfrsr7nchaod1mich M1	crgcsphotaodfiltqav3M1.a1	ARM_CRG lv2
ARM EPC M1	2023-01-06 to 2024-02-14	epcfrsr7nchaod1mich M1	epccsphotaodfiltqav3M1.a1	ARM_La_Jolla lv2
ARM GUC M1	2021-04-30 to 2023-06-16	gucfrsr7nchaod1mich M1	guccsphotaodfiltqav3M1.a1	ARM_Gothic lv2
ARM HOU M1	2021-01-20 to 2022-10-01	houmfrsr7nchaod1mich M1	houcsphotaodfiltqav3M1.a1	ARM_LaPorte lv2
NOAA TBL	2016-08-25 to 2019-11-28	tbl_yyyymmdd.aod yyyymmdd.nc	N/A (Not an ARM site)	Table_Mountain lv2

2.2 ARM mobile facility campaigns

The seven AMF deployments provided highly instrumented, temporary measurements of clouds, aerosols, and radiative fluxes in regions with significant data gaps.

- **Bankhead National Forest (BNF) campaign:** Initiated in September 2024 at the U.S. Forest Service Black Warrior Work Center (northwestern Alabama, USA) and surrounding areas, this multi-year campaign investigates complex interactions among vegetation, aerosols, and clouds over complex terrain (Kuang et al., 2026). The collocated comparison data were from AERONET site "ARM_BNF" (Table 1).
- **Cloud And Precipitation Experiment at Kennaook (CAPE-k):** Conducted at the Kennaook/Cape Grim Baseline Air Pollution Station (KCG) in Tasmania (Australia) from April 2024 through October 2025, this campaign investigated pristine marine boundary layer (MBL) air masses and the seasonal cycles of MBL clouds in an under-sampled region (Mace et al., 2023). The collocated comparison data were from AERONET site "ARM_KCG" (Table 1).

https://doi.org/10.5194/egusphere-2026-5957
Preprint. Discussion started: 3 November 2026
© Author(s) 2026. CC BY 4.0 License.

- **Coast-Urban-Rural Atmospheric Gradient Experiment (CoURAGE):** Conducted in and around Baltimore, Maryland (USA), from December 2024 to November 2025, this campaign investigated the interplay among urban heat islands, coastal meteorological dynamics, and rural-to-urban aerosol gradients (Davis et al., 2024). The collocated comparison data were from AERONET site "ARM_CRG" (Table 1).
- **Eastern Pacific Cloud Aerosol Precipitation Experiment (EPCAPE):** Conducted in La Jolla, California (USA), from February 2023 to February 2024, this campaign investigated the radiative properties and aerosol–cloud interactions of marine stratocumulus clouds undergoing the transition from clean marine backgrounds to urban pollution (Russell et al., 2021). The collocated comparison data were from AERONET site "ARM_La_Jolla" (Table 1).
- **Surface Atmosphere Integrated Field Laboratory (SAIL):** Conducted in the mountainous East River Watershed near Crested Butte, Colorado (USA), from September 2021 to June 2023, this campaign investigated coupled atmosphere-through-bedrock processes in a mid-latitude continental interior (Feldman et al., 2023). The collocated comparison data were from AERONET site "ARM_Gothic" (Table 1).
- **Tracking Aerosol Convection Interactions Experiment (TRACER):** Conducted in the urban-coastal region of Houston, Texas (USA), from October 2021 to September 2022, this campaign investigated the convective cloud life cycle and the impacts of urban and industrial aerosols on convective storm intensity (Jensen et al., 2025). The collocated comparison data were from AERONET site "ARM_LaPorte" (Table 1).
- **Oliktok Point (OLI)**: Conducted in coastal region of Alaska (USA), this deployment investigated atmospheric processes and surface–atmosphere interactions affecting Arctic sea ice. The OLI comparison is somewhat abbreviated since shortly after the MFRSR 7 channel was added the AMF deployment at Oliktok was completed. The OLI observatory was located approximately 260 km from the fixed NSA C1 site. The collocated comparison data were from AERONET site "ARM_Oliktok_AK" (Table 1).

2.3 NOAA Table Mountain Test Facility

This Facility is an atmospheric and solar radiation monitoring station located on a large, flat-topped mesa approximately 10 km north of Boulder, Colorado (USA). Operated by the NOAA Global Monitoring Laboratory, the site functions as a key station within the SURFRAD network (e.g., Augustine et al., 2000, 2005). Characterized by a semi-arid climate and sparse grassland land cover, the site provides excellent local horizon visibility and high clear-sky frequency. The NOAA data used in this study were collected from 25 August 2016 to 28 November 2019. The collocated comparison data were from AERONET site "Table_Mountain" (Table 1).

https://doi.org/10.5194/egusphere-2026-5957
Preprint. Discussion started: 3 November 2026
© Author(s) 2026. CC BY 4.0 License.

2.4 Instrumental differences

While these sites and campaigns span highly diverse environments, they all feature collocated MFRSR and Cimel instruments. Notably, these instruments rely on fundamentally different optical designs: the MFRSR utilizes a hemispherical receptor periodically occluded by a rotating shadowband, whereas the Cimel utilizes a direct sun-pointing design. Furthermore, the two instruments employ distinct radiometric calibration protocols and trace gas absorption corrections. Because gas absorption features can be comparable in magnitude to the AOD within the near-infrared spectrum (1625-1640 nm) (e.g., Livingston et al., 2005), discrepancies between MFRSR and Cimel AOD products may stem, in part, from these calibration and correction differences. The next section outlines these calibrations and gas corrections, focusing on the MFRSR methodology.

3 Calibrations and gas corrections for AOD

3.1 Radiometric calibration

In-field radiometric MFRSR calibration is performed using twice-daily Langley regressions that linearly relate the logarithm of measured direct irradiance to the optical air mass (am, Fig. 2). The am quantifies the atmospheric path length between the Sun and the surface, where a value of unity (1.0) represents the Sun at the zenith position. This in-field calibration technique has been applied successfully for nearly three decades (e.g., Harrison and Michalsky, 1994; Michalsky et al., 2001; Augustine et al., 2003; Michalsky and Long, 2016). Because individual daily regressions exhibit noise from short-term atmospheric variability, several weeks of operational measurements are aggregated to filter out high-variance data. Only regression datasets demonstrating low statistical variability are retained to establish a stable daily calibration. Applying these stabilized calibration coefficients to the MFRSR measurements yields continuous time series of total optical depth (TOD) for each spectral channel. The corresponding AOD is derived using:

$$AOD = TOD - \tau_{Rayleigh} - \tau_{gas} \quad (1)$$

where $\tau_{Rayleigh}$ is the Rayleigh optical depth due to molecular scattering (a function of surface pressure), and τ_{gas} is the total gas absorption optical depth (a function of air mass).

https://doi.org/10.5194/egusphere-2026-5957
Preprint. Discussion started: 3 November 2026
© Author(s) 2026. CC BY 4.0 License.

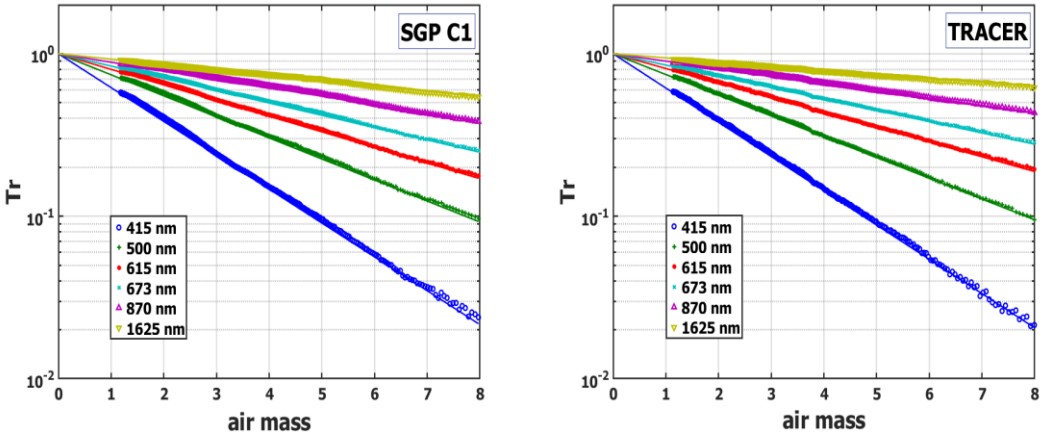


Figure 2. Examples of MFRSR Langley plots at six channels for the SGP C1 site (22 July 2025) and during the TRACER campaign (18 August 2021). To illustrate the expected monotonic wavelength dependence (where shorter wavelengths exhibit steeper slopes and larger optical depths), these plots depict the atmospheric transmittance (Tr), the signal for each channel normalized by the y-intercept of the Langley regression line, which naturally approaches unity at zero air mass.

In-field radiometric Cimel calibration is performed every 6 to 12 months via intercomparison with master instruments at the Goddard Space Flight Center (GSFC). These master instruments are calibrated using the Langley method at the Mauna Loa Observatory in Hawaii (e.g., Toledano et al., 2018). Situated at an altitude of 3397 m, this observatory frequently experiences clean, free-tropospheric air masses above the marine boundary layer, particularly during morning hours.

3.2 Gas correction

Gas absorption varies significantly across the targeted wavelength channels. Ozone (O_3) absorption impacts three visible channels centered at 500, 615, and 673 nm. The corresponding O_3 optical depth is derived from columnar ozone abundances retrieved by the Total Ozone Mapping Spectrometer (TOMS) or the Ozone Monitoring Instrument (OMI). Conversely, absorption features for carbon dioxide (CO_2), methane (CH_4), and water vapor (H_2O) overlap between 1605–1655 nm spectral region (Fig. 3).

https://doi.org/10.5194/egusphere-2026-5957
Preprint. Discussion started: 3 November 2026
© Author(s) 2026. CC BY 4.0 License.

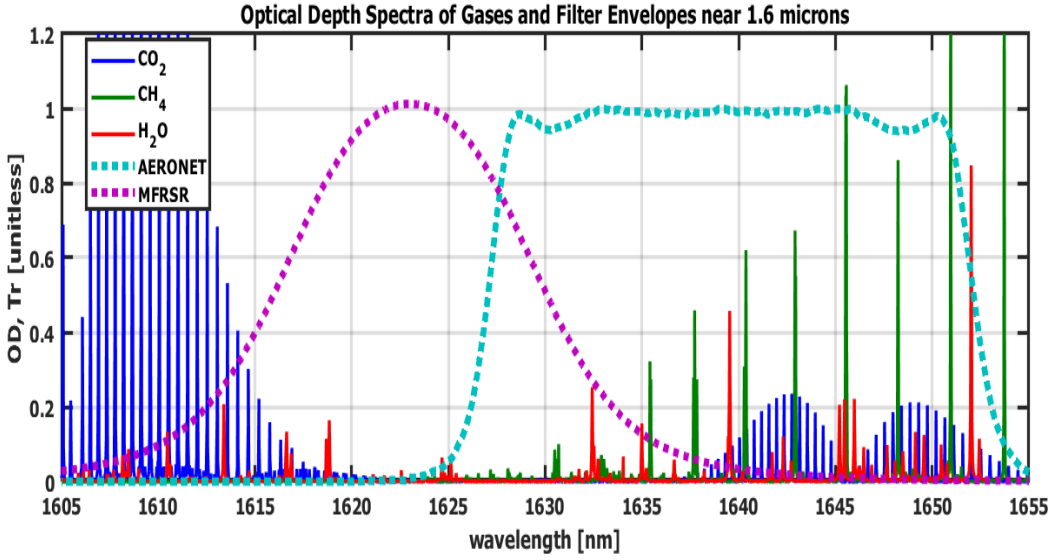


Figure 3. Optical depth spectra between 1605-1655 nm for CO_2 (blue), CH_4 (green), and H_2O (red). Filter transmission envelopes are denoted for the 7-ch MFRSR channel (dashed magenta) and the AERONET Cimel channel (dashed light blue).

To quantify the gas absorption for CO_2 and CH_4, a three-step process is adapted from the previous studies (e.g., Ortiz de Galisteo et al., 2009; Korkin et al., 2025). First, the high-resolution spectral transmittance, $T_{gas}(\lambda)$, for a given wavelength (λ) and air mass is computed using the Line-By-Line Radiative Transfer Model (LBLRTM; e.g., Clough et al., 2005):

$$T_{gas}(\lambda) = exp\left[-\tau_{gas}(\lambda) am\right] \quad (2)$$

where the subscript "gas" denotes either for CO_2 or CH_4.

Second, the channel-averaged gas transmittance, $\overline{T_{gas}(\lambda)}$, is determined by convolving $T_{gas}(\lambda)$ with the non-uniform instrumental filter response function, $T_{filter}(\lambda)$, shown in Figure 3:

$$\overline{T_{gas}} = \int T_{gas}(\lambda)\, T_{filter}(\lambda)\, d\lambda \quad (3)$$

Finally, this average transmittance is converted into an average channel gas absorption optical depth scaled for the specified air mass:

$$\overline{\tau_{gas}} = -ln\left[\overline{T_{gas}}\right]/am \quad (4)$$

The necessity of Eqs. (2)–(4) for discrete narrow-line structures (e.g., Fig. 3) becomes apparent when considering the effect of averaging contiguous spectral intervals where optical depths vary abruptly and substantially. For example, averaging two

https://doi.org/10.5194/egusphere-2026-5957
Preprint. Discussion started: 3 November 2026
© Author(s) 2026. CC BY 4.0 License.

adjacent spectral regions with hypothetical optical depths of 0 and 2×10^6 yields a mean optical depth of 1×10^6, implying an opaque medium. This result is physically incorrect because the transparent region (optical depth of 0) permits radiation transmission. Conversely, the corresponding transmittances for these two intervals are 1 and 0, which average to 0.5 and yield an effective optical depth of 0.69. This aligns with the physical expectation that both spectral elements contribute to the net transmission. This behavior is a direct consequence of Jensen's inequality, which states that the logarithm of the mean does not equal the mean of the logarithm.

Because LBLRTM-based computations of channel-averaged gas absorption entail prohibitive computational runtime during operational processing, these evaluations were executed *a priori* across the anticipated air mass domain (from 1 to 6) to construct look-up tables (LUTs). Subsequent parameterization of the average gas absorption is achieved via a least-squares quadratic regression, mapping the discrete LUT space to a continuous second-order polynomial representation:

$$\overline{\tau_{gas}} = a_{gas} + b_{gas}\, am + c_{gas}\, am^2 \quad (5)$$

This three-step methodology is adapted to quantify the channel-averaged absorption of H_2O by substituting the air mass with the column-integrated precipitable water vapor (PWV). Integrating concurrent observations from ARM infrastructure, this absorption is evaluated over a PWV range of 0 to 10 cm to construct site-specific LUTs that parameterize water vapor attenuation across diverse atmospheric path lengths. These LUTs are parameterized through an exponential and second-order polynomial formulation:

$$\overline{\tau_{H_2O}} = \exp\left[a_{H_2O} + b_{H_2O}\, PWV + c_{H_2O}\, PWV^2\right] \quad (6)$$

The fitting parameters *a*, *b*, and *c* (Eqs. 5,6) are available as field-level attributes in the "mfrsr7nchaod1" Netcdf files noted in Table 1. Two key points regarding the highlighted parameterizations (5)-(6) should be noted. First, the parameterization accuracy is high, with fit residuals remaining below 10^{-5} in optical depth for all gases (CO_2, CH_4, H_2O). Second, the total absorption optical depth for these gases is, on average, approximately 0.01, rendering it can be comparable in magnitude (constituting up to 70%) to the mean MFRSR AODs obtained for clean observational conditions (Fig. 4).

https://doi.org/10.5194/egusphere-2026-5957
Preprint. Discussion started: 3 November 2026
© Author(s) 2026. CC BY 4.0 License.

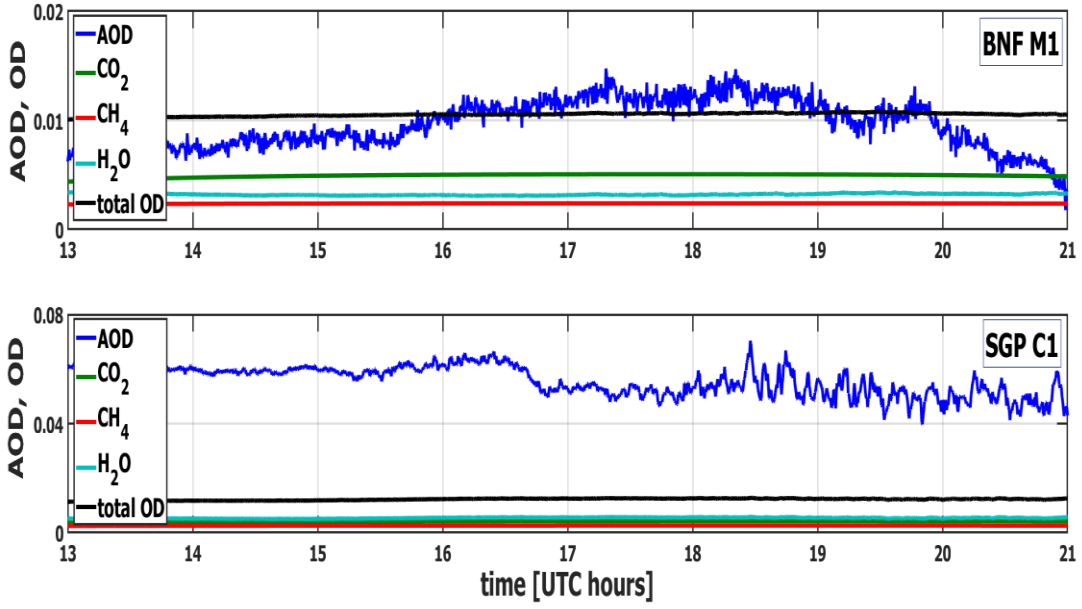


Figure 4. Examples of AODs, individual (CO_2, CH_4, H_2O) and total gas optical depths (ODs) for small and moderate aerosol loadings observed at the BNF M1 (September 7, 2025) and SGP C1 (July 22, 2025) sites.

Giles et al. (2019) established the AERONET Version 3 optical depth corrections for the 1640 nm Cimel channel to account for gas absorption by H_2O, CO_2, and CH_4. The AERONET H_2O correction utilizes a linear formulation, $\overline{\tau_{H_2O}} = A_{H_2O} + B_{H_2O}\, PWV$, where A_{H_2O} and B_{H_2O} represent filter-specific and instrument-unique coefficients. Conversely, the CO_2 and CH_4 corrections apply constant absorption coefficients scaled by local atmospheric pressure, expressed as $\overline{\tau_{CO_2}} = 0.0087\, P/P_0$ and $\overline{\tau_{CH_4}} = 0.0047\, P/P_0$, where P is the atmospheric pressure at the station's elevation and P_0 is the standard sea-level reference pressure. It should be emphasized that these corrections are appropriate only for the 1640 nm Cimel channel with specific features of gas absorption (Fig. 3). Thus, they are not directly applicable to the 7-ch MFRSR channel (Fig. 3). Moreover, significant variation in MFRSR filters requires unique filter-by-filter corrections.

The MFRSR AOD at 1625 nm is computed using Eq. (1) along with the gas corrections described in Eqs. (5) and (6). In Sect. 4, the computed MFRSR AOD (1625 nm) is compared against the reference Cimel AOD (1640 nm). The comparison relies on scatterplots and key statistical metrics obtained across the ARM fixed sites, field campaigns, and NOAA Table Mountain Test Facility highlighted in Sect. 2.

https://doi.org/10.5194/egusphere-2026-5957
Preprint. Discussion started: 3 November 2026
© Author(s) 2026. CC BY 4.0 License.

4 Evaluation of MFRSR AOD

4.1 ARM fixed research sites

The radiometric MFRSR calibration relies on the Langley method (Sect. 3.1), which requires an unobstructed, cloud-free line of sight between the Sun and the ground-based instrument. At the subtropical ENA site, such clear-sky intervals occur infrequently due to a persistently high total cloud fraction. This cloudiness follows an annual cycle that peaks in winter (about 0.85) and reaches a minimum in late summer (about 0.70) (e.g., Wood et al., 2015; Dong et al., 2022). Consequently, clear-sky intervals suitable for Langley regressions are limited to about 30% of the operational period or less. Despite these stringent clear-sky constraints, direct scatterplot comparisons (Fig. 5a) and statistical analyses (Table 2) demonstrate good agreement between the MFRSR and Cimel AODs. The majority of data points cluster tightly along the 1:1 line (Fig. 5a), yielding a regression slope near unity (0.98) and a small root-mean-square error (RMSE ~ 0.013; Table 2).

Table 2. Parameters of linear regressions (Fig. 5) obtained for Cimel AOD (1640 nm) and MFRSR AOD (1625 nm) at four ARM fixed sites, NSA Oliktok field campaign, and NOAA Table Mountain Test Facility (last column). The root mean square error (RMSE) and number of points (N) are also included.

	ENA	NSA(C1)	NSA(Oliktok)	SGP(C1)	SGP(E13)	NOAA
Slope	0.98	0.93	0.82	0.92	0.83	1.00
Intercept	-0.001	0.002	0.003	0.000	-0.002	0.002
Mean(y)	0.045	0.018	0.027	0.035	0.026	0.017
Mean(x)	0.047	0.017	0.023	0.038	0.035	0.016
Bias (y-x)	-0.002	0.001	-0.002	-0.004	-0.007	0.002
RMSE	0.013	0.008	0.003	0.013	0.007	0.004
N	25,665	5,222	681	70,541	69,429	17,105

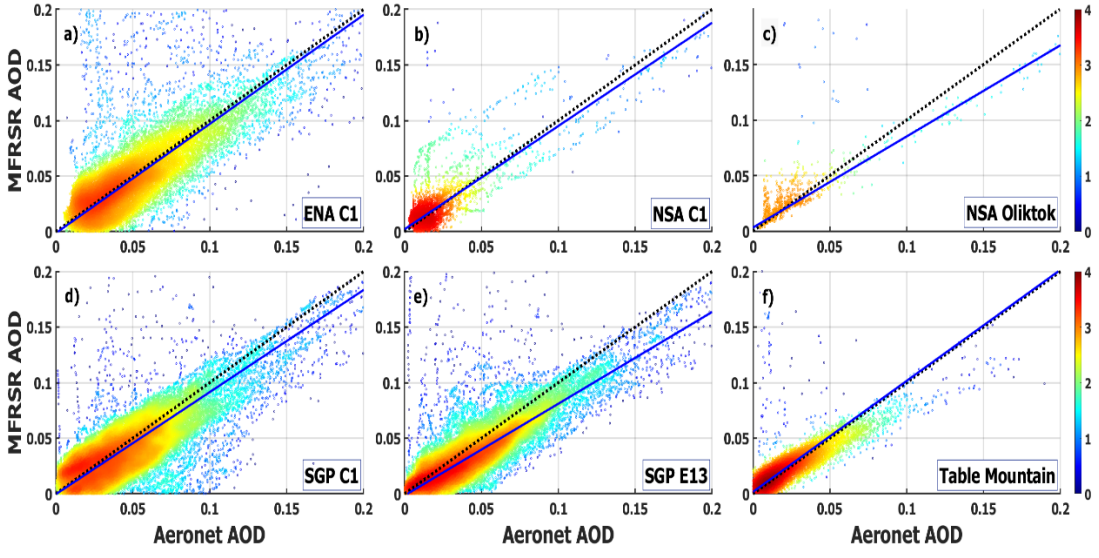


Figure 5. Density plots of MFRSR AOD (1625 nm) versus Cimel AERONET AOD (1640 nm) measured at four ARM fixed sites and one field campaign: ENA C1(a), NSA C1(b), NSA Oliktok(c), SGP C1(d), SGP E13 (e); and NOAA Table Mountain Test Facility(f). The color is a relative density plot on log-scale with blue color representing low point density (0 = 10^0, one point only) and red color indicating high point density (4 = 10^4 points).

https://doi.org/10.5194/egusphere-2026-5957
Preprint. Discussion started: 3 November 2026
© Author(s) 2026. CC BY 4.0 License.

Similar to the ENA site, the high-latitude NSA C1 site exhibits a distinct annual cycle of cloudiness. The monthly mean total cloud fraction ranges from a minimum of approximately 0.55 in March to a maximum near 0.95 from late summer through early autumn (August–October; Dong et al., 2010). However, the NSA C1 site also experiences highly seasonal daytime availability restricted by polar day and night cycles, as well as high solar zenith angles (>70°) associated with a low solar elevation near the horizon. These two factors, combined with the moderate-to-large cloud fractions, introduce substantial high-latitude observational challenges, notably reducing the number of periods favorable for AOD measurements. Consequently, the number of data points used for the AOD evaluation at the NSA C1 site is approximately one fifth that for the ENA C1 site (Table 2) over comparable observation periods of approximately 5 years each (Sect. 2.1). Nevertheless, the overarching impact of these sampling constraints on the overall AOD statistics remains low; the NSA C1 RMSE is small (0.008) and the linear regression slope is close to unity (0.93; Fig. 5b; Table 2). At the NSA Oliktok Point site, a smaller data sample also appears to be unaffected by these constraints, yielding a well-aligned AOD comparison on average (Fig. 5c; Table 2).

Cloudiness at the mid-latitude SGP site peaks in winter (up to 0.55) and reaches a minimum in summer (about 0.40) (e.g., Xi et al., 2010), providing clear-sky Langley conditions during 45% or more of the deployment. However, fair-weather cumulus clouds driven by daytime land heating occur frequently at the SGP site during summer days (e.g., Berg and Kassianov, 2008; Gustafson et al., 2020). These localized clouds are partly responsible for minor discrepancies between the AODs measured by the collocated MFRSR C1 and MFRSR E13 instruments (Fig. 5d,e; Table 2). Although the small spatial separation between these two radiometers ensures they sample the same regional background atmosphere under stable, horizontally homogeneous conditions, small-scale spatial variations of clouds and aerosol can still induce localized differences in the direct-beam path. Beyond these atmospheric small-scale variations, instrumental aspects, such as minor leveling misalignments and instrument tilts, may contribute to the slight differences between AODs measured by these MFRSRs. Despite these combined atmospheric and instrumental factors, AODs from both MFRSRs remain in reasonable agreement with the Cimel reference; regression slopes are close to unity (0.92 for C1 and 0.83 for E13), RMSE values are low (0.013 and 0.007, respectively), and the absolute bias remains below 0.01 (Table 2).

4.2 NOAA Table Mountain Test Facility

The performance of the upgraded MFRSR was evaluated via a comparison against the collocated Cimel (Fig. 5f, Table 2). Regression statistics demonstrate excellent agreement between the MFRSR AOD at 1625 nm and the Cimel AOD at 1640 nm, yielding an ideal slope of 1.00, a negligible intercept of 0.002, a low RMSE of 0.004, and a low bias of 0.002 (Table 2). This high agreement is primarily attributed to the favorable site location with a high clear-sky frequency that maximizes unobstructed direct solar beam measurements. Furthermore, rigorous instrument calibration and meticulous maintenance mitigate potential instrumental artifacts and structural errors, such as minor MFRSR leveling misalignments and sensor tilt, confirming that the 1625 nm MFRSR channel achieves high-fidelity AOD measurements under near ideal operational conditions.

https://doi.org/10.5194/egusphere-2026-5957
Preprint. Discussion started: 3 November 2026
© Author(s) 2026. CC BY 4.0 License.

4.3 ARM mobile facility campaigns

The five low-altitude field campaigns encompass a diverse range of conditions, ranging from pristine marine boundary layers (CAPE-k) to complex coastal-urban-rural settings (CoURAGE) and dense forested regimes (BNF). Regression analyses across these five deployments reveal strong correlation between MFRSR and Cimel AODs (Fig. 6a-d,f; Table 3); the RMSE remains within 0.01, and the regression slopes sit near unity (Table 3). A systematic minor underestimation by the MFRSR occurs across four of these deployments (BNF, CAPE-k, CoURAGE, and EPCAPE; Fig. 5a-d), manifest as a slight negative bias of approximately (-0.01) (Table 3). This bias likely stems from instrumental MFRSR issues, including minor leveling misalignments and instrument tilt, which went undetected by MFRSR automated data screening. We plan to resolve these issues in collaboration with the ARM Data Quality Office (e.g., Peppler et al., 2016) in our future study using standard corrections (e.g., Alexandrov et al., 2007).

Table 3. The same as Table 2 except for six ARM campaigns.

	BNF	CAPE-k	CoURAGE	EPCAPE	SAIL	TRACER
Slope	0.99	1.01	1.00	1.03	1.17	0.95
Intercept	-0.009	-0.010	-0.010	-0.011	-0.001	-0.003
Mean(y)	0.019	0.028	0.018	0.024	0.016	0.038
Mean(x)	0.028	0.038	0.028	0.034	0.014	0.043
Bias (y-x)	-0.009	-0.010	-0.010	-0.01	0.002	-0.005
RMSE	0.006	0.008	0.008	0.006	0.005	0.008
N	9,435	6,274	11,805	11,160	12,032	16,901

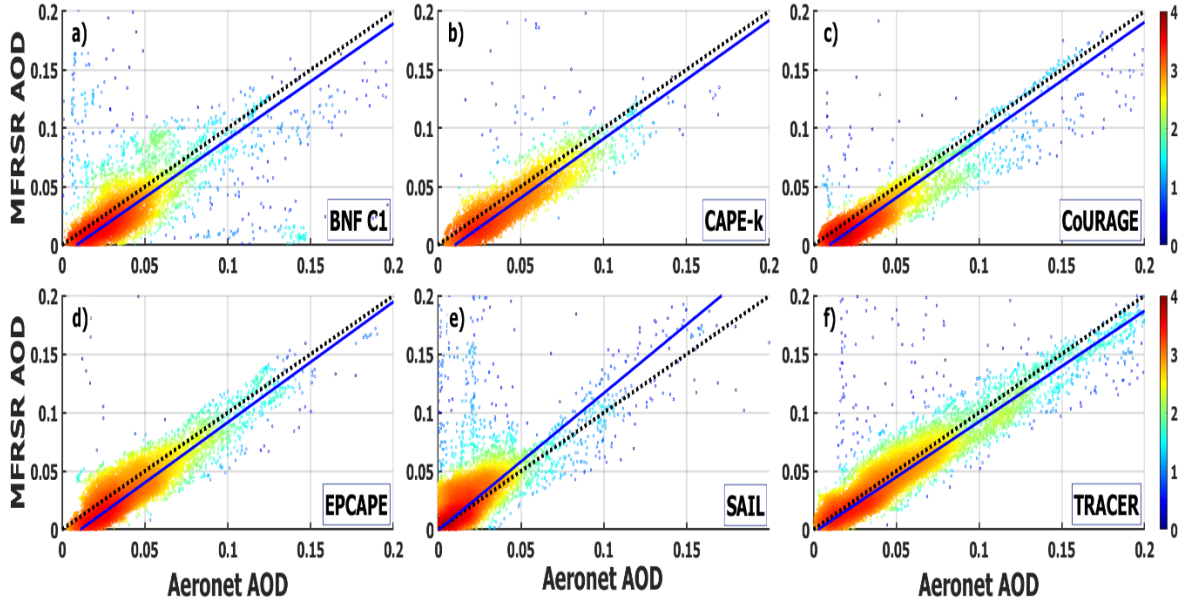


Figure 6. The same as Figure 5 except for six ARM campaigns.

https://doi.org/10.5194/egusphere-2026-5957
Preprint. Discussion started: 3 November 2026
© Author(s) 2026. CC BY 4.0 License.

In contrast to the high-latitude NSA site, the high-altitude SAIL campaign does not experience highly seasonal daytime availability restricted by polar day and night cycles, nor does it face frequently high solar zenith angles (> 70°) associated with low solar elevations near the horizon. Consequently, the number of data points used for the AOD evaluation during SAIL is substantially larger than that for the NSA C1 site (Tables 2 and 3). However, similar to the NSA site, the SAIL campaign experiences sub-freezing temperatures, seasonal solid precipitation, and blowing snow during the cold season. These conditions introduce observational challenges, notably potential rime and frost accumulation on the radiometers. This accumulation likely exerts differential effects on the hemispherical MFRSR versus the sun-pointing Cimel. Thus, such occasional accumulation can drive the statistical outliers visible in the corresponding scatter plot (Fig. 6e) and cause the regression slope to deviate from unity (Table 3). Nevertheless, the impact of these outliers is not pronounced in the SAIL data, as the AOD RMSE and bias remain small (0.005 and 0.002, respectively).

5 Conclusions

This study evaluates a new near-infrared (1625 nm) aerosol optical depth (AOD) product generated from data offered by upgraded Multifilter Rotating Shadowband Radiometers (MFRSRs). The new AOD product is generated by integrating solar transmittance, line-by-line gas absorption spectra, and instrumental filter response function, following established methodologies (e.g., Ortiz de Galisteo et al., 2009; Korkin et al., 2025). The evaluation of the new AOD product utilizes integrated datasets collected at four Atmospheric Radiation Measurement (ARM) fixed sites: Southern Great Plains (SGP C1 and E13; Sisterson et al., 2016), North Slope of Alaska (NSA C1; Verlinde et al., 2016), and Eastern North Atlantic (ENA C1; Wood et al., 2015). Additionally, datasets collected during seven ARM field campaigns are incorporated: (1) Bankhead National Forest (BNF M1; Kuang et al., 2026), (2) Cloud And Precipitation Experiment at Kennaook (CAPE-k; Mace et al., 2023), (3) Coast-Urban-Rural Atmospheric Gradient Experiment (CoURAGE; Davis et al., 2024), (4) Eastern Pacific Cloud Aerosol Precipitation Experiment (EPCAPE; Russell et al., 2021), (5) Surface Atmosphere Integrated Field Laboratory (SAIL; Feldman et al., 2023), (6) Tracking Aerosol Convection Interactions Experiment (TRACER; Jensen et al., 2025), and (7) Oliktok Point. Datasets from one National Oceanic and Atmospheric Administration (NOAA) Surface Radiation Budget (SURFRAD) Table Mountain Test Facility (e.g., Augustine et al., 2000, 2005) are also integrated into this evaluation.

Using AODs measured at 1640 nm wavelength by collocated and coincident Aerosol Robotic Network (AERONET) Cimel sun photometers as a reference, this study evaluates the new MFRSR AOD (1625 nm) across the ARM sites and campaigns characterized by diverse environmental regimes and moderate-to-high cloud cover. Despite these challenging observational conditions, the MFRSR AOD (1625 nm) demonstrates a strong correlation with the reference Cimel AOD (1640 nm) at nearly all permanent and mobile ARM deployments considered here. The MFRSR and Cimel AOD values, on average, cluster tightly along the 1:1 line; linear regression analyses yield slopes close to unity (0.82-1.03), root-mean-square errors (RMSE) mostly below 0.013, and absolute biases generally within 0.01. Furthermore, we demonstrate that excellent agreement between the

https://doi.org/10.5194/egusphere-2026-5957
Preprint. Discussion started: 3 November 2026
© Author(s) 2026. CC BY 4.0 License.

MFRSR and Cimel AOD values can be achieved under near-ideal operational conditions characterized by a high clear-sky frequency, rigorous instrument calibration, and meticulous maintenance. Under these optimal conditions observed at the NOAA Table Mountain Test Facility, an ideal linear regression slope of 1.00 and an exceptionally low RMSE of 0.004 are obtained.

By demonstrating the high accuracy of the MFRSR AOD (1625 nm), this study establishes a reliable foundation for characterizing coarse aerosols (CA), such as sea salt and desert dust, across diverse global locations with the upgraded MFRSR deployments. Characterization of CA can, for example, improve the understanding of interactions among desert dust storms, extreme heat and urban growth observed during a new ARM-supported campaign (e.g., Aiken et al., 2026). Beyond aerosol characterization, the upgraded MFRSR data can advance surface and cloud retrievals by utilizing the upgraded MFRSR measurements of near-infrared (NIR) downwelling irradiances. These measurements provide critical spectral constraints for characterizing underlying surface types and deriving high-resolution NIR surface albedo (e.g., McFarlane et al., 2011). Because surface albedo variations significantly confound cloud retrievals from ground-based radiation measurements, these enhanced MFRSR constraints can improve retrievals of cloud properties (e.g., Chiu et al., 2006; LeBlanc et al., 2015; Riihimaki et al., 2021) and thus expand the utility of the MFRSR network for integrated aerosol-cloud-surface research.

Code and data availability

The ARM MFRSR AOD datastreams are freely available through the ARM data archive (Table 1). Only AOD values passing all embedded ARM QC tests and not identified as bad or suspect in ARM Data Quality Reports were used. The SURFRAD MFRSR AOD datastreams are freely available through the NOAA GML SURFAD archive under “aod”. Only AOD values passing the SURFRAD cloud-screen test were used. The AERONET Cimel sun photometer data are freely available through the AERONET Download Tool or the AERONET webservice, and also through the ARM data archive with the instrument name CSPHOT (Cimel Sun Photometer) (Table 1). The AERONET level 1.5 AOD data are ingested into ARM Netcdf files as datastream “csphotaodfiltv3”, while the AERONET level 2 AOD data are ingested into ARM datastream “csphotaodfiltqav3”. There may be minor differences between the AERONET and ARM datastreams due to independent reprocessing schedules. In our study level 1.5 AOD values are only used when level 2 AOD values are unavailable. Cloud-screened quality-assessed level 2 AOD data (v3) was used whenever post-calibrated data was available, otherwise cloud-screened level 1.5 AOD (v3) data was used. In all cases, the distance between MFRSR and Cimel instruments is less than 100 meters. Times are synchronized to UTC via NTP and/or GPS. Nearest-neighbor matching was applied with a threshold of less than 20-second to ensure good coincidence between measurement times.

https://doi.org/10.5194/egusphere-2026-5957
Preprint. Discussion started: 3 November 2026
© Author(s) 2026. CC BY 4.0 License.

Author contributions

Conceptualization: EK and CJF with inputs from JJM, JAA, HT. Data processing: ELC, GLG, GH, BS. Formal analysis: EK and CJF. Writing (original draft): EK. Writing (review and editing): EK and CJF with inputs from JCB, JES, DZ, LM, JMC.

Competing interests

The authors declare that they have no conflict of interest.

Disclaimer

Publisher's note: Copernicus Publications remains neutral with regard to jurisdictional claims made in the text, published maps, institutional affiliations, or any other geographical representation in this paper. While Copernicus Publications makes every effort to include appropriate place names, the final responsibility lies with the authors. Views expressed in the text are those of the authors and do not necessarily reflect the views of the publisher.

Acknowledgements

This research was supported by the US Department of Energy (DOE), Office of Science Biological and Environmental Research (BER), as part of the Atmospheric Radiation Measurement (ARM) user facility. This research was also supported by the Global Monitoring Laboratory of the National Oceanic and Atmospheric Administration (NOAA). The Pacific Northwest National Laboratory is operated for the DOE by the Battelle Memorial Institute under contract DE-AC05-76RL01830.

The authors express their sincere appreciation to the technicians, instrument mentors, scientists, and the broader ARM, NOAA and AERONET communities for their essential efforts in operating and maintaining the ground-based instruments worldwide.

Financial support

This research was supported by Battelle (grant no. DE-AC05-76RL01830). Brookhaven National Laboratory was supported by the Office of Science BER in the DOE, through the US DOE (contract no. DE-SC0012704). Portions of this research were conducted at the National Weather Center, University of Oklahoma through Argonne National Laboratory, subcontract No. 4F-60252 between UCHICAGO ARGONNE, LLC, an Illinois limited liability company, operator of Argonne National Laboratory and herein called the "Laboratory", acting under Prime Contract No. DE-AC02-06CH11357, as amended, with the

https://doi.org/10.5194/egusphere-2026-5957
Preprint. Discussion started: 3 November 2026
© Author(s) 2026. CC BY 4.0 License.

United States Government (called the "Government") represented by the U. S. DOE, and THE BOARD OF REGENTS OF THE UNIVERSITY OF OKLAHOMA (called the Subcontractor), an educational institution.

References

Aiken, T., et al.: Desert-Urban System Integrated Atmospheric Monsoon (DUSTIEAIM) in the Southwestern United States Science Plan, Tech. rep., 10.2172/2572202, 2026.

Alexandrov, M. D., Kiedron, P., Michalsky, J. J., Hodges, G., Flynn, C. J., and Lacis, A. A.: Optical depth measurements by shadow band radiometers and their uncertainties, Appl. Opt., 46, 8027–8038, https://doi.org/10.1364/AO.46.008027, 2007.

Augustine, J. A., Cornwall, C. R., Hodges, G. B., Long, C. N., Medina, C. I., and DeLuisi, J. J.: An automated method of MFRSR calibration for aerosol optical depth analysis with application to an Asian dust outbreak over the United States, J. Appl. Meteorol., 42, 266–278, https://doi.org/10.1175/1520-0450(2003)042<0266:AAMOMC>2.0.CO;2, 2003.

Augustine, J. A., DeLuisi, J. J., and Long, C. N.: SURFRAD–A National Surface Radiation Budget Network for Atmospheric Research, Bull. Amer. Meteorol. Soc., 81, 2341–2358, https://doi.org/10.1175/1520-0477(2000)081<2341:SANSRB>2.3.CO;2, 2000.

Augustine, J. A., Hodges, G. B., Dutton, E. G., Michalsky, J. J., and Harrison, W. E.: An Update on SURFRAD—The GCOS Surface Radiation Budget Network for the Continental United States, J. Atmos. Oceanic Technol., 22, 1460–1472, https://doi.org/10.1175/JTECH1806.1, 2005.

Balmes, K. A., Riihimaki, L. D., Wood, J., Flynn, C., Theisen, A., Ritsche, M., Ma, L., Hodges, G. B., and Herrera, C.: Evaluation of the hyperspectral radiometer (HSR1) at the Atmospheric Radiation Measurement (ARM) Southern Great Plains (SGP) site, Atmos. Meas. Tech., 17, 3783–3807, https://doi.org/10.5194/amt-17-3783-2024, 2024.

Berg, L. K. and Kassianov, E. I.: Temporal variability of fair-weather cumulus statistics at the ACRF SGP site, J. Climate, 21, 3344–3358, https://doi.org/10.1175/2007JCLI2266.1, 2008.

Chiu, J. C., Marshak, A., Knyazikhin, Y., Wiscombe, W., Barker, H., Barnard, J. C., and Luo, Y.: Remote sensing of cloud properties using ground-based measurements of zenith radiance, J. Geophys. Res., 111, D16201, https://doi.org/10.1029/2005JD006843, 2006.

Clough, S. A., Shephard, M. W., Mlawer, E. J., Delamere, J. S., Iacono, M. J., Cady-Pereira, K., Boukabara, S., and Brown, P. D.: Atmospheric radiative transfer modeling: a summary of the AER codes, J. Quant. Spectrosc. Radiat. Transfer, 91, 233–244, https://doi:10.1016/j.jqsrt.2004.05.058, 2005.

Davis, K., Zaitchik, B., Asa-Awuku, A., Bou-Zeid, E., Baidar, S., Boxe, C., Brewer, W. A., Chiao, S., Damoah, R., DeCarlo, P., Demoz, B., Dickerson, R., Giometto, M., Gonzalez-Cruz, J., Jensen, M., Kuang, C., Lamer, K., Li, X., Lombardo, K., Miles, N., Niyogi, D., Pan, Y., Peters, J., Ramamurthy, P., Peng, W., Richardson, S., Sakai, R., Waugh, D., and Zhang, J.: Coastal-Urban-Rural Atmospheric Gradient Experiment (CoURAGE) Science Plan, Tech. Rep. DOE/SC-ARM-24-016, Oak

https://doi.org/10.5194/egusphere-2026-5957
Preprint. Discussion started: 3 November 2026
© Author(s) 2026. CC BY 4.0 License.

Ridge National Laboratory (ORNL), Oak Ridge, TN (United States). Atmospheric Radiation Measurement (ARM) Data Center, https://doi.org/10.2172/2429693, 2024.

Dong, X., Xi, B., Crosby, K., Long, C. N., Stone, R. S., and Shupe, M. D.: A 10 year climatology of Arctic cloud fraction and radiative forcing at Barrow, Alaska, J. Geophys. Res., 115, D17212, https://doi.org/10.1029/2009JD013489, 2010.

Dong, X., Zheng, X., Xi, B., and Xie, S.: A Climatology of Midlatitude Maritime Cloud Fraction and Radiative Effects, J. Climate, 35, 6931–6947, https://doi.org/10.1175/JCLI-D-22-0290.1, 2022.

Dusek, U., Frank, G. P., Hildebrandt, L., Curtius, J., Schneider, J., Walter, S., Chand, D., Drewnick, F., Hings, S., Jung, D., Borrmann, S., and Andreae, M. O.: Size matters more than chemistry for cloud-nucleating ability of aerosol particles, Science, 312, 1375–1378, DOI: 10.1126/science.1125261, 2006.

Feldman, D. R., Aiken, A. C., Boos, W. R., Carroll, R. W. H., Chandrasekar, V., Collins, W. D., Cox, C. J., de Boer, G., DeMott, P. J., Fan, J., Flugge, A. M., Gochis, D. J., Hill, T. C. J., Hodshire, A. L., Johnson, E., Joseph, E., Levin, E. J. T., Lundquist, J. K., O'Brien, D., Rasmussen, R. M., Ritsche, M. T., Rowell, N. P., Sharp, S. D., Shupe, M. D., Smith, J. N., Sullivan, R. C., Tornow, F., Varble, A. C., and Williams, I. N.: The Surface Atmosphere Integrated Field Laboratory (SAIL) Campaign, Bull. Amer. Meteorol. Soc., 104, E2192–E2222, https://doi.org/10.1175/BAMS-D-22-0049.1, 2023.

García, R. D., Barreto, Á., Cachorro, V. E., González-Sicilia, P., Léon-Luis, S., Álvarez-Hernández, A., Bustos, J. J., Ramos, R., Almansa, F., Álvarez-Losada, Ó., González, Y., Rivas, P. P., and Torres, C. J.: Impact of spectral aerosol radiative forcing at the Izaña observatory during the August 2023 extreme wildfires, Atmos. Meas. Tech., 19, 3151–3167, https://doi.org/10.5194/amt-19-3151-2026, 2026.

Giles, D. M., Sinyuk, A., Sorokin, M. G., Schafer, J. S., Smirnov, A., Slutsker, I., Eck, T. F., Holben, B. N., Lewis, J. R., Campbell, J. R., Welton, E. J., Korkin, S. V., and Lyapustin, A. I.: Advancements in the Aerosol Robotic Network (AERONET) Version 3 database – automated near-real-time quality control algorithm with improved cloud screening for Sun photometer aerosol optical depth (AOD) measurements, Atmos. Meas. Tech., 12, 169–209, https://doi.org/10.5194/amt-12-169-2019, 2019.

Gustafson, W. I. and Coauthors: The Large-Eddy Simulation (LES) Atmospheric Radiation Measurement (ARM) Symbiotic Simulation and Observation (LASSO) activity for continental shallow convection, Bull. Amer. Meteor. Soc., 101, E462–E479, https://doi.org/10.1175/BAMS-D-19-0065.1, 2020.

Harrison, L. and Michalsky, J.: Objective algorithms for the retrieval of optical depths from ground-based measurements, Appl. Opt., 33, 5126–5132, https://opg.optica.org/ao/abstract.cfm?URI=ao-33-22-5126, 1994.

Holben, B. N., Eck, T. F., Slutsker, I., Tanré, D., Buis, J. P., Setzer, A., Vermote, E., Reagan, J. A., Kaufman, Y. J., Nakajima, T., Lavenu, F., Jankowiak, I., and Smirnov, A.: AERONET—A federated instrument network and data archive for aerosol characterization, Remote Sens. Environ., 66, 1–16, 10.1016/S0034-4257(98)00031-5, 1998.

Jaeglé, L., Quinn, P. K., Bates, T. S., Alexander, B., and Lin, J.-T.: Global distribution of sea salt aerosols: new constraints from in situ and remote sensing observations, Atmos. Chem. Phys., 11, 3137–3157, https://doi.org/10.5194/acp-11-3137-2011, 2011.

https://doi.org/10.5194/egusphere-2026-5957
Preprint. Discussion started: 3 November 2026
© Author(s) 2026. CC BY 4.0 License.

Jensen, M. P., Flynn, J. H., Gonzalez-Cruz, J. E., Judd, L. M., Kollias, P., Kuang, C., McFarquhar, G. M., Powers, H., Ramamurthy, P., Sullivan, J., Aiken, A. C., Alvarez, S. L., Argay, P., Argrow, B., Bell, T. M., Boyer, D., Brooks, S. D., Bruning, E. C., Brunner, K., Butterworth, B., Calmer, R., Cappa, C. D., Chakrabarty, R. K., Chandrasekar, V., Chao, C.-Y., Chen, B., China, S., Collins, D. R., Collis, S. M., Crowell, S., Porto, R. D., Boer, G. de, Deng, M., Dexheimer, D., Drager, A. J., Du, X., Dubey, M. K., Dzambo, A. M., Etten-Bohm, M., Fan, J., Farley, R., Feng, Y.-C., Feng, Y., Fenn, M., Ferrare, R. E., Flusche, S., Fridlind, A. M., Galewsky, J., Gamarro, H., Gardner, S., Ghate, V. P., Giangrande, S. E., Griffin, R. J., Griggs, T., Gronoff, G. P., Grover, M., Gaugenti, M., Guo, F., Gupta, S., Hu, J., Huang, Y., Jackson, R. C., Hair, J. W., Johnson, K. L., Kasparoglu, S., Klein, P., Kotsakis, A. E., Kumar, J., Kumjian, M. R., Lamer, K., Lappin, F. M., Lei, Z., Li, J., Li, R., Li, Y., Logan, T., Lombardo, K., Luke, E. P., Mages, Z., Matthews, A. A., Matthews, B. H., Mayol-Bracero, O., Matsui, T., McKeown, K. E., Mehra, M., Mei, F., Meskidzhe, N., Nguyen, C., Nielsen, E. R., Nowotarski, C. J., Oaks, D., Oktem, R., Oue, M., Park, J. M., Partida, N., Patil, S., Pena, J. C., Petters, M. D., Phoenix, D. B., Puthserry, J. V., Rapp, A. D., Romps, D. M., Roots, M., Rosenfeld, D., Saleeby, S. M., Savala, P., Sedlacek, A. J., Sharma, M., Sheesley, R., Shingler, T. J., Shrestha, S., Singh, A., Smith, E. N., Smith, J. N., Smith, S., Snyder, J., Spicer, E., Spinei, E., Spychala, M., Steir, P., Storm, M. R., Subba, T., Treserras, B. P., Trojanowski, R., Theisen, A., Thompson, S. A., Twigg, L., Uin, J., Ulinski, A. R., Heever, S. van den, Lier-Walqui, M. van, Varble, A. C., Wagner, T. J., Wakeen, J., Wales, N. A., Walter, P. J., Wang, D., Wang, J., Wood, L., Wang, Y., Wolde, M., Yoon, S., Young, M. H., Zawadowicz, M. A., Zhang, Q., Zhou, A., Zhu, Z., and Zhu, Z.: Studying aerosol, clouds, and air quality in the coastal urban environment of southeastern Texas, Bull. Amer. Meteorol. Soc., 106, E1821–E1841, https://doi.org/10.1175/BAMS-D-23-0331.1, 2025.

Karanikolas, A., Kouremeti, N., Campanelli, M., Estellés, V., Momoi, M., Kumar, G., Nyeki, S., and Kazadzis, S.: Intercomparison of aerosol optical depth retrievals from GAW-PFR and SKYNET sun photometer networks and the effect of calibration, Atmos. Meas. Tech., 17, 6085–6105, https://doi.org/10.5194/amt-17-6085-2024, 2024.

Kassianov, E., Flynn, C. J., Barnard, J. C., Ermold, B. D., and Comstock, J. M.: Shortwave Array Spectroradiometer-Hemispheric (SAS-He): design and evaluation, Atmos. Meas. Tech., 17, 4997–5013, https://doi.org/10.5194/amt-17-4997-2024, 2024.

Kassianov, E., Pekour, M., and Barnard, J.: Aerosols in central California: Unexpectedly large contribution of coarse mode to aerosol radiative forcing, Geophys. Res. Lett., 39, L20806, https://doi.org/10.1029/2012GL053469, 2012.

Korkin, S., Sayer, A.M., Ibrahim, A., and Lyapustin, A.: A practical guide to coding line-by-line trace gas absorption in Earth's atmosphere. J Quant Spectrosc Radiat Transf., 337, https://doi.org/10.1016/j.jqsrt.2025.109345, 2025.

Kuang, C., Giangrande, S. E., Serbin, P. P., Campbell, P., Elsaesser, G. S., Gentine, P., Heus, T., Hickmon, N. L., Oue, M., Peters, J. M., Raghunathan, G. N., Ritsche, M. T., Smith, J. N., Spychala, M., Steiner, A. L., and Theisen, A.: The U.S. DOE ARM User Facility establishes a new site for studies of land–aerosol–cloud interactions in the Southeastern United States, Bull. Amer. Meteorol. Soc., 107, E1–E8, https://doi.org/10.1175/BAMS-D-25-0072.1, 2026.

https://doi.org/10.5194/egusphere-2026-5957
Preprint. Discussion started: 3 November 2026
© Author(s) 2026. CC BY 4.0 License.

Laszlo, I. and Liu, H.: EPS Aerosol Optical Depth (AOD) Algorithm theoretical basis document, NOAA NESDIS STAR Technical Report, available at: https://www.star.nesdis.noaa.gov/pub/smcd/akhuff/ACC_Product_Documentation/AOD_ATBD_Enterprise.pdf (last access: 31 October 2026), 2022.

LeBlanc, S. E., Pilewskie, P., Schmidt, K. S., and Coddington, O.: A spectral method for discriminating thermodynamic phase and re trieving cloud optical thickness and effective radius using trans mitted solar radiance spectra, Atmos. Meas. Tech., 8, 1361–1383, https://doi.org/10.5194/amt-8-1361-2015, 2015.

Levy, R. C., Gupta, P., Shi, Y. R., Remer, L. A., Kim, M., Oo, M. M., Mattoo, S., Torres, O., and Jethva, H.: A GEO-LEO imager data set for characterizing rapid changes of global aerosol properties, J. Geophys. Res.-Atmos., 131, e2025JD046107, https://doi.org/10.1029/2025JD046107, 2026.

Liu, F., Pan, Z., Rosenfeld, D., and Zhu, Y.: Fine and coarse aerosols control of cloud water by evaporation-precipitation dynamics, npj Clim. Atmos. Sci., 8, 299, https://doi.org/10.1038/s41612-025-01193-8, 2025.

Livingston, J. M., Schmid, B., Russell, P. B., Eilers, J. A., Kolyer, R. W., et al.: Retrieval of ozone column content from airborne Sun photometer measurements during SOLVE II: comparison with coincident satellite and aircraft measurements, Atmos. Chem. Phys., 5, 2035–2054, https://doi.org/10.5194/acp-5-2035-2005, 2005.

Mace, G., Marchand, R., Keywood, M., Protat, A., Humphries, R., Fiddes, S., McCluskey, C., Siems, S., Huang, Y., May, P., and Ma, P.-L.: Cloud and Precipitation Experiment at Kennaook (Cape-K) Science Plan, Tech. Rep. DOE/SC-ARM-23-011, Oak Ridge National Laboratory (ORNL), Oak Ridge, TN (United States). Atmospheric Radiation Measurement (ARM) Data Center, https://doi.org/10.2172/1986088, 2023.

McFarlane, S. A., Gaustad, K. L., Mlawer, E. J., Long, C. N., and Delamere, J.: Development of a high spectral resolution surface albedo product for the ARM Southern Great Plains central f acility, Atmos. Meas. Tech., 4, 1713–1733, https://doi.org/10.5194/amt-4-1713-2011, 2011.

Michalsky, J. J. and Kiedron, P. W.: Moderate spectral resolution solar irradiance measurements, aerosol optical depth, and solar transmission, from 360 to 1070 nm, using the refurbished rotating shadow band spectroradiometer (RSS), Atmos. Meas. Tech., 15, 353–364, https://doi.org/10.5194/amt-15-353-2022, 2022.

Michalsky, J. J. and Long, C. N.: ARM Solar and Infrared Broadband and Filter Radiometry, Meteorol. Monogr., 57, 16.1–16.15, https://doi.org/10.1175/AMSMONOGRAPHS-D-15-0031.1, 2016.

Michalsky, J. J., Denn, F., Flynn, C., Hodges, G., Kiedron, P., Koontz, A., Schlemmer, J., and Schwartz, S. E.: Climatology of aerosol optical depth in north central Oklahoma: 1992–2008, J. Geophys. Res., 115, D07203, https://doi.org/10.1029/2009JD012197, 2010.

Michalsky, J. J., Schlemmer, F. A., Berkheiser, W. E., Berndt, J. L., Harrison, L. C., Laulainen, N. S., Larson, N. R., and Barnard, J. C.: Multi-year measurements of aerosol optical depth in the Atmospheric Radiation Measurement and Quantitative Links programs, J. Geophys. Res., 106, 12099–12107, https://doi.org/10.1029/2001JD900096, 2001.

https://doi.org/10.5194/egusphere-2026-5957
Preprint. Discussion started: 3 November 2026
© Author(s) 2026. CC BY 4.0 License.

Miller, M. A., Nitschke, K., Ackerman, T. P., Ferrell, W. R., Hickmon, N., and Ivey, M.: The ARM Mobile Facilities, Meteorol. Monogr., 57, 9.1–9.15, https://doi.org/10.1175/AMSMONOGRAPHS-D-15-0051.1, 2016.

Nakajima, T., Campanelli, M., Che, H., Estellés, V., Irie, H., Kim, S.-W., Kim, J., Liu, D., Nishizawa, T., Pandithurai, G., Soni, V. K., Thana, B., Tugjsurn, N.-U., Aoki, K., Go, S., Hashimoto, M., Higurashi, A., Kazadzis, S., Khatri, P., Kouremeti, N., Kudo, R., Marenco, F., Momoi, M., Ningombam, S. S., Ryder, C. L., Uchiyama, A., and Yamazaki, A.: An overview of and issues with sky radiometer technology and SKYNET, Atmos. Meas. Tech., 13, 4195–4218, https://doi.org/10.5194/amt-13-4195-2020, 2020.

Ortiz de Galisteo, J. P., Cachorro, V. E., Toledano, C., Rodríguez, E., Berjón, A., and de Frutos, A. M.: Error source in AOD retrieval from filter radiometer data in the UV due to filter band function, J. Aerosol Sci., 40, 597–602, 10.1016/j.jaerosci.2009.03.006, 2009.

Peppler, R. A., Kehoe, K. E., Monroe, J. W., Theisen, A. K., and Moore, S. T.: The ARM Data Quality Program, Meteorol. Monogr., 57, 12.1–12.14, https://doi.org/10.1175/AMSMONOGRAPHS-D-15-0039.1, 2016.

Riihimaki, L. D., Flynn, C., McComiskey, A., Lubin, D., Blanchard, Y., Chiu, J. C., Feingold, G., Feldman, D. R., Gristey, J. J., Herrera, C., Hodges, G., Kassianov, E., LeBlanc, S. E., Marshak, A., Michalsky, J. J., Pilewskie, P., Schmidt, S., Scott, R. C., Shea, Y., Thome, K., Wagener, R., and Wielicki, B.: The Shortwave Spectral Radiometer for Atmospheric Science: Capabilities and Applications from the ARM User Facility, Bull. Amer. Meteorol. Soc., 102, E539–E554, https://doi.org/10.1175/BAMS-D-19-0227.1, 2021.

Russell, L. M., Cappa, C. D., de Szoeke, S. P., Fairall, C. W., Feingold, G., Freedman, A., Gasso, S., Goldstein, A. H., Modini, P., Prather, K. A., Quinn, P. K., Seinfeld, J. H., Sorooshian, A., Zhang, Q., and Ziemann, P. J.: Eastern Pacific Cloud Aerosol Precipitation Experiment (EPCAPE) Science Plan, Tech. Rep. DOE/SC-ARM-21-009, Oak Ridge National Laboratory (ORNL), Oak Ridge, TN (United States). Atmospheric Radiation Measurement (ARM) Data Center, https://doi.org/10.2172/1804710, 2021.

Sawyer, V., Levy, R. C., Mattoo, S., Shi, Y. R., Kim, M., Remer, L. A., and Cureton, G.: An updated VIIRS dark target aerosol product for continuity with MODIS: assessing regional aerosol trends, Front. Environ. Sci., 13, 1602145, https://doi.org/10.3389/fenvs.2025.1602145, 2025.

Shinozuka, Y., Redemann, J., Livingston, J. M., Russell, P. B., Clarke, A. D., Howell, S. G., Freitag, S., O'Neill, N. T., Reid, E. A., Johnson, R., Ramachandran, S., McNaughton, C. S., Kapustin, V. N., Brekhovskikh, V., Holben, B. N., and McArthur, L. J. B.: Airborne observation of aerosol optical depth during ARCTAS: vertical profiles, inter-comparison and fine-mode fraction, Atmos. Chem. Phys., 11, 3673–3688, https://doi.org/10.5194/acp-11-3673-2011, 2011.

Sisterson, D. L., Peppler, R. A., Cress, T. S., Lamb, P. J., and Turner, D. D.: The ARM Southern Great Plains (SGP) Site, Meteorol. Monogr., 57, 6.1–6.14, https://doi.org/10.1175/AMSMONOGRAPHS-D-16-0004.1, 2016.

Toledano, C., González, R., Fuertes, D., Cuevas, E., Eck, T. F., Kazadzis, S., Kouremeti, N., Gröbner, J., Goloub, P., Blarel, L., Román, R., Barreto, Á., Berjón, A., Holben, B. N., and Cachorro, V. E.: Assessment of Sun photometer Langley calibration

https://doi.org/10.5194/egusphere-2026-5957
Preprint. Discussion started: 3 November 2026
© Author(s) 2026. CC BY 4.0 License.

at the high-elevation sites Mauna Loa and Izaña, Atmos. Chem. Phys., 18, 14555–14567, https://doi.org/10.5194/acp-18-14555-2018, 2018.

Verlinde, J., Zak, B. D., Shupe, M. D., Ivey, M. D., and Stamnes, K.: The ARM North Slope of Alaska (NSA) Sites, Meteorol. Monogr., 57, 8.1–8.13, https://doi.org/10.1175/AMSMONOGRAPHS-D-15-0023.1, 2016.

Vu, T. V., Delgado-Saborit, J. M., and Harrison, R. M.: Review: particle number size distributions from seven major sources and implications for source apportionment studies, Atmos. Environ., 122, 114–132, https://doi.org/10.1016/j.atmosenv.2015.09.027, 2015.

Wang, S., Brock, C., Kondragunta, S., Laszlo, I., and McDonald, B.: Evaluating aerosol optical depth retrieved from VIIRS using global scale, multi-seasonal airborne observations, J. Geophys. Res.-Atmos., 129, e2023JD040700, https://doi.org/10.1029/2023JD040700, 2024.

Wood, R., Wyant, M., Bretherton, C. S., Rémillard, J., Kollias, P., Fletcher, J., Stemmler, J., de Szoeke, S., Yuter, S., Miller, M., Mechem, D., Tselioudis, G., Chiu, J. C., Mann, J. A. L., O'Connor, E. J., Hogan, R. J., Dong, X., Miller, M., Ghate, V., Jefferson, A., Min, Q., Minnis, P., Palikonda, R., Albrecht, B., Luke, E., Hannay, C., and Lin, Y.: Clouds, aerosols, and precipitation in the marine boundary layer: an ARM Mobile Facility deployment, Bull. Amer. Meteorol. Soc., 96, 419–440, https://doi.org/10.1175/BAMS-D-13-00180.1, 2015.

Xi, B., Dong, X., Minnis, P., and Khaiyer, M. M.: A 10 year climatology of cloud fraction and vertical distribution derived from both surface and GOES observations over the DOE ARM SGP site, J. Geophys. Res., 115, D12124, https://doi.org/10.1029/2009JD012800, 2010.

Yin, J., Pan, Z., Mao, F., Rosenfeld, D., and Zhu, Y.: Large effects of fine and coarse aerosols on tropical deep convective systems throughout their lifecycle, npj Clim. Atmos. Sci., 7, 195, https://doi.org/10.1038/s41612-024-00739-6, 2024.